Physics of Plasmas ARTICLE scitation.org/journal/php

Effect analysis of angular momentum on coaxial multipactor with 1D3V statistical modeling

Cite as: Phys. Plasmas **29**, 103105 (2022); doi: 10.1063/5.0101112
Submitted: 29 May 2022 · Accepted: 11 September 2022 ·
Published Online: 20 October 2022

Shu Lin,[1,2,3] Hao Qu,[1,2] Patrick Wong,[3] Peng Zhang,[3] John Verboncoeur,[3] Huan Zhong,[1,2] Yonggui Zhai,[1,2] Meng Cao,[1,2] Hongguang Wang,[1,2] and Yongdong Li[1,2,a)]

AFFILIATIONS

[1]Key Laboratory for Physical Electronics and Devices of the Ministry of Education, Xi'an Jiaotong University, Xi'an 710049, China
[2]School of Electronic Science and Engineering, Xi'an Jiaotong University, Xi'an 710049, China
[3]Department of Electrical and Computer Engineering, Michigan State University, East Lansing, Michigan 48824, USA

[a)]**Author to whom correspondence should be addressed:** leyond@mail.xjtu.edu.cn

ABSTRACT

How does the multipactor threshold voltage vary when two semi-infinite parallel plates are bent into coaxial lines? This topic with respect to the geometric effect on multipactor formation is essential for the optimal design of multipactor-free microwave systems. It requires accurate multipactor threshold analysis of the coaxial lines with the consideration of electron angular momentum, which is not considered in most multipactor theoretical approaches for efficient threshold calculations. To address this effect from the perspective of multipactor threshold analysis, this work presents an improved implementation of the multipactor statistical modeling (1D3V modeling) by constructing the joint probability density function with angular emissions and impacts of secondary electrons included. On that basis, a multipactor susceptibility chart of coaxial lines is conducted and compared with the experimental results, and multipactor threshold voltage for varying ratios of outer to inner conductor radii (radius ratio) is calculated to quantitatively investigate the effect of electron angular momentum. The results indicate that the 1D3V modeling can achieve fairly good agreement with the experimental result and relatively better accuracy of threshold calculation at first multipactor orders with comparison to the 1D1V result which only regards the radial momentum. With different variations of the threshold voltage from the 1D1V result, the 1D3V result reaches its minimum at a specific radius ratio before the sudden rise, and the discrepancy becomes more significant for the high-order multipactor, revealing the indispensable effect of angular momentum on the coaxial multipactor. The intricacies of the mechanism analysis will be further explored in the paper.

I. INTRODUCTION

Multipactor discharge is an undesired electromagnetic phenomenon sustained by resonant secondary electron emissions, which, in turn, are caused by the synchronized electron acceleration and impact on the device walls with the radio frequency (RF) field.[1] It ubiquitously takes place in powerful microwave devices widely applied to accelerator structures, vacuum electronics, and space-borne telecommunications,[2–4] resulting in signal interference,[5] performance degradation,[6] and even permanent equipment damage.[7] Regarding this potential threat with catastrophic hazards, multipactor prevention is conventionally required to guarantee the operational durability and reliability of microwave systems, especially for the modern aerospace industry. Accordingly, there is growing research interest in efficient surface treatments which adopt inertial materials[8,9] or micro-porous structures[10–12] on the device surfaces for the suppression of secondary electron emissions.

Thorough investigation of the geometric effect on multipactor formation benefits the optimal design for multipactor prevention but also requires accurate methods of multipactor threshold calculation. For this reason, recent multipactor research still retains substantial interest in developing useful multipactor predictive techniques. Besides the particle-in-cell[13] (PIC) and Monte-Carlo[14] (MC) methods, multipactor theoretical work has also achieved good developments and applications with novel theories[15–17] and methods[18–20] for multipactor investigation. Amongst them, the multipactor statistical theory is one critical and accurate method for multipactor mechanism analysis and threshold calculation, for its capability of fully regarding the stochastic characteristic of secondary electron emission from the probabilistic perspective.[21,22] The statistical modeling is not as good as the PIC and MC simulations in practical applicability comparatively, but it is capable of obtaining satisfactory efficiency and accuracy in multipactor threshold prediction. With rapid developments in the past

decade, multipactor statistical modeling has been widely applied to mechanism analysis and threshold calculation of the two-surface multipactor discharge in typical microwave devices with the singlecarrier or multicarrier[23] signal excitation as well as the single-surface multipactor discharge on a dielectric surface.[24,25]

With a view to the underlying dependence of multipactor susceptibility on the geometry of the device, the statistical modeling was extended to investigate the multipactor dynamic process in the coaxial lines, which is of great significance because of its common adoption in microwave engineering. Besides statistical modeling, the practicality of the coaxial lines also attracted plenty of other theoretical[15,26] and numerical[27,28] works of multipactor. Nonetheless, current multipactor theoretical analysis with coaxial geometry is mostly based on a one-dimensional (1D) electron trajectory formula that is approximately derived with the perturbation method.[29,30] This approximate derivation fundamentally promotes the modeling convenience and applicability, even capable of including the space charge effect,[26] but the resultant calculation error determined by the validity of the derivation approximation inevitably exerts a strong effect on the modeling feasibility.[31] To solve this common problem and improve the modeling accuracy, an implementation method of multipactor statistical modeling through numerically tracking electron motions is further introduced to remove its obstinate dependence on an analytical solution of electron motions.[31]

However, similar to other analytical work, the present multipactor statistical analysis still deals with multipactor breakdown as a 1D problem and only considers the component of electron motions normal to the surface (abbreviated as the 1D1V model below). However, secondary electrons from consecutive collisions on the device surface are generated with angular emission in real multipactor dynamics.[32] Electron transversal motions due to angular emissions will result in oblique impacts and accordingly engender more secondary emissions[33] on the device surfaces, especially when electron impact energy exceeds 50 eV. On the other hand, electron transition and acceleration are also hampered with smaller emission velocity in the radial direction for the probability transfer from the normal velocity to the transverse component. Thus, it is of great necessity to further study multipactor threshold variation under these conflicting effects caused by the angular momenta of multipactor electrons, especially for multipactor breakdown of the coaxial lines or the circular waveguides[34] where the curved surface possibly enhances the contribution of angular impacts.

Hence, this research is dedicated to investigating the effects of electron angular momentum on multipactor formation in the coaxial lines. It is focused on quantitative threshold analysis of the coaxial multipactor using an improved statistical model (called the 1D3V model below), which regards both angular emissions and impacts of multipactor electrons based on a previous numerical construction algorithm of the joint probability density function (JPDF).[31] The content is organized as follows. First, the 1D3V multipactor statistical modeling and the related probability analysis of electron transition, including the improved numerical algorithm for the JPDF construction with electron angular momentum considered, are detailed in Sec. II. On that basis, a multipactor susceptibility chart for typical 50 Ω coaxial lines and multipactor threshold calculations for coaxial lines with different radius ratios (the ratio of outer to inner conductor radii) are conducted using the 1D1V and 1D3V statistical models for comparative analysis in Sec. III. The mechanism analysis with the calculation of the average impact angle is provided as well. Finally, the consequent conclusion and further discussion are provided in Sec. IV.

II. 1D3V STATISTICAL MODELING

This section describes our revised nonstationary statistical model of multipactor taking into account the azimuthal component of electron velocity in addition to the radial component. After introducing the basic definitions of the statistical modeling, the JPDF is constructed by numerically tracking the multipactor electron trajectories in the coaxial geometry under the action of the prescribed transverse electric and magnetic (TEM) fields with random emission velocities and angles. This JPDF is then used to calculate the probability distribution of electron transit times, and the transition probability and the population of secondary electrons are next obtained, yielding information on the effect of this additional azimuthal electron velocity and, hence, angular momentum on multipactor formation. Because of the addition of angular emission for the multipactor electrons and, hence, consequently angular impact with the electrodes, the underlying mechanism and the threshold determination of the coaxial multipactor are both altered. We will explore these changes and compare the calculation results of this 1D3V model to the conventionally used 1D1V model to ascertain the importance of including the azimuthal degree of freedom.

Note that electron motions in the azimuthal direction inevitably give rise to the spatial transport of multipactor electrons at different azimuthal positions in the coaxial lines. However, the resulting variation of electron population is compensated for the symmetric development of coaxial multipactor. Therefore, multipactor statistical modeling developed in this section merely investigates multipactor evolution at a constant position but taking both normal and transverse electron motion into consideration. This is also the reason why it is abbreviated as the 1D3V statistical modeling in the above statement. Meanwhile, the space charge effect is still neglected with our focus set on the initial onset condition of multipactor formation in the coaxial lines, for the initial field induced by low-density space charge is negligible for electron motions.

A. Basic definitions and classifications

For better depiction of the statistical modeling, the labels "*o*" and "*i*" are used to differentiate the related parameters of the outer and inner conductor surface, respectively. Meanwhile, it also adopts "*ds*" and "*ss*" in the subscripts to denote the double-sided (DS) impacts (*o*–*i* or *i*–*o* trajectories) and single-sided (SS) impacts (*o*–*o* or *i*–*i* trajectories) with different emission surfaces for all the relevant parameters as illustrated in Fig. 1. For example, the constituted labels of "*ds*, *o*" and "*ss*, *o*" represent the DS and SS impacts for electrons emitted from the outer conductor surface separately. Meanwhile, main relevant definitions for the statistical modeling are listed in Table I, and specific derivations will be further detailed in this section. Note that the variable τ in parenthesis refers to electron transit time (actually the transit phase of electron impacts), and the emission phase φ_s is periodic with respect to the field phase φ for the period of 2π. Meanwhile, the above statistical definitions are also depending on the electron trajectory ξ, which is correlated to the frequency and the voltage amplitude of the rf field (f and V_{rf}) as well as the radii of the outer and inner conductor (R_o and R_i). The gap between the outer and

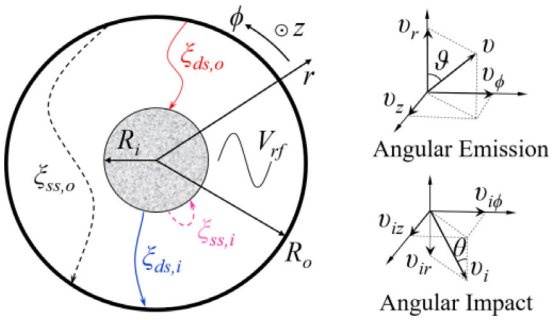

FIG. 1. Illustration of multipactor formation in the coaxial lines and the velocity components for angular emissions and impacts of multipactor electrons. ξ_{ds} and ξ_{ss} refer to the double-sided (solid) and single-sided (dashed) impacts, and the additional subscripts "o" and "i" represent different trajectories with outer and inner emission separately.

inner conductor is denoted as d ($d = R_o - R_i$) and can be normalized as λ with

$$\lambda = \frac{\omega d}{v_\omega}, \tag{1}$$

where ω equals to $2\pi f$ and v_ω refers to the radial oscillation velocity, yielding

$$v_\omega = \frac{eV_{rf}}{m_e \omega r_s \ln \gamma}, \tag{2}$$

where m_e is the electron mass, γ is the radius ratio ($\gamma = R_o/R_i$), and r_s is the radial location at electron emission and set with R_i or R_o.

B. The JPDF with random angular emission

To provide an accurate description of the multipactor process, electron angular emissions with directional anisotropy are commonly adopted for multipactor theoretical models. The following Maxwellian and cosine distribution functions are assumed for random emission velocity v and angle ϑ (cf. Fig. 1) of secondary electrons, respectively, as in the previous statistical literatures,[32,35]

$$f_v(v) = \frac{2}{(2\pi v_t^2)^{3/2}} \exp\left(-\frac{v^2}{2v_t^2}\right), \tag{3}$$

$$f_\vartheta(\vartheta) = 2\cos\vartheta, \tag{4}$$

where v_t represents the thermal velocity of secondary emissions. Note that the thermal spread of emission velocity also affects the onset condition of multipactor, and here, the corresponding thermal energy $m_e v_t^2/2$ is chosen to be 1.5 eV as previous statistical literatures.[22,30] For the convenience of statistical modeling, the following two-dimensional (2D) distribution function for the emission velocity of secondary electrons is further derived from the above equations (see more details in Refs. 32 and 35) and expressed in cylindrical coordinates with further normalization as

$$f(u_r, u_\phi) = \frac{\sqrt{2}u_r}{\chi^2 \pi^{3/2}} \exp\left(-\frac{u_r^2 + u_\phi^2}{4\chi^2}\right) K_0\left(\frac{u_r^2 + u_\phi^2}{4\chi^2}\right), \tag{5}$$

where u_r and u_ϕ are the radial and azimuthal emission velocities v_r and v_ϕ normalized to the oscillation velocity v_ω, respectively, and χ accounts for the ratio of v_t to v_ω.

Note that electron emission randomness in the axial direction is neglected here because of the minimal axial diffusion of multipactor electrons at the initial formation stage of multipactor. This has been proved with the random walk analysis in Ref. 28. It is worth emphasizing that electron motion in the axial direction is still regarded here with the axial emission velocity v_z set constant at zero. From the physical essence, the JPDF (denoted as $G(\tau|\varphi_s)$ in Table I) represents the probability density of electron impacts with transit time τ and emission phase φ_s, and it is commonly calculated through transferring the randomness from electron emission velocity to electron transit time. However, the previous analytical approach is not applicable here because of the field nonuniformity in coaxial lines as mentioned above. Thus, the following JPDF construction procedure, based on the previous numerical algorithm for the 1D1V multipactor modeling, adds the above 2D distribution of the emission velocity into consideration.

Similar to the previous 1D construction algorithm, the time-domain argument of the JPDF is also segmented into evenly spaced intervals. At the same time, the 2D velocity distribution is meshed into small velocity grids that are delimited by uniform segmentations of the

TABLE I. Main relevant definitions for the statistical modeling.

$C_{o/i}(\varphi)$	Emission rate (electrons/radian) of surface o/i at the incident field phase φ
$I_{o/i}(\varphi)$	Impact rate (electrons/radian) of surface o/i at the incident field phase φ
$N(\varphi)$	Total electron population inside the gap at the incident field phase φ
$G_{ds/ss,\ o/i}(\tau\|\varphi_s)$	Probability density for DS/SS impacts of electrons emitted from surface o/i with transit time τ and emission phase φ_s
$\sigma_{ds/ss,\ o/i}(\tau\|\varphi_s)$	Incident secondary emission yield for DS/SS impacts of electrons emitted from surface o/i with transit time τ and emission phase φ_s
$K_{ds/ss,\ o/i}(\tau\|\varphi_s)$	Population density of secondary electron for DS/SS impacts of electrons emitted from surface o/i with transit time τ and emission phase φ_s
$P_{ds/ss,\ o/i}(\varphi_s)$	Overall probability of DS/SS impacts for electrons emitted from surface o/i with emission phase φ_s
$S_{ds/ss,\ o/i}(\varphi_s)$	Overall population of secondary electron for DS/SS impacts of electrons emitted from surface o/i with emission phase φ_s

velocity distribution in both the radial and azimuthal directions as illustrated in Fig. 2(a). For either DS or SS impacts, the probability assignment of each velocity grid is determined by the transit times of electrons emitted with the 2D velocity pairs at the grid nodes, which are generally located at the intersection of four adjacent grids and possess their partial probability amount. Apparently, this distribution segmentation is more complicated than that in the previous 1D algorithm which merely requires the electron transit time corresponding to the representative velocities of the velocity section in the 1D velocity distribution; however, this is still quite suitable albeit more complicated for the statistical modeling here with 2D velocity distribution.

Taking the velocity grid g_1 composed of four nodes N_1, N_2, N_3, and N_4 in Fig. 2(a) for example, the corresponding transit time for the velocity pairs in these grid nodes $N_1(u_r^j, u_\phi^k)$, $N_2(u_r^{j+1}, u_\phi^k)$, $N_3(u_r^j, u_\phi^{k+1})$, and $N_4(u_r^{j+1}, u_\phi^{k+1})$ are denoted as τ_1, τ_2, τ_3, and τ_4, respectively. The probability amount $\Delta p(g_1)$ held by the grid g_1, which signifies the probability for electrons emitted within the velocity ranges of $[u_r^j, u_r^{j+1}]$ and $[u_\phi^k, u_\phi^{k+1}]$ delimited by g_1, can be calculated through the following integral:

$$\Delta p(g_1) = \int_{u_r^j}^{u_r^{j+1}} \int_{u_\phi^k}^{u_\phi^{k+1}} f(u_r, u_\phi) du_r du_\phi, \tag{6}$$

where the velocity ranges in both directions are depending on the grid mesh. Each grid node roughly takes up about one-quarter of the probability amount of each adjacent velocity grid surrounding the grid node; thus, the total probability amount p_b which refers to the probability for electrons emitted with the 2D velocity pair of the grid g_b held by the node N_l is written as

$$p_l = \frac{1}{4} \sum_{m \in M}^{n_M} \Delta p(g_m), \tag{7}$$

where M and n_M are the index collection and the total number of the velocity grids intersected at the node N_b, respectively. As illustrated in Fig. 2(b), electron transit time of four grid nodes τ_{1-4} have different locations for the discrete velocity grid g_1, and thus the corresponding probability amount $\Delta p(g_1)$ is evenly assigned to the time interval $\Delta\tau_{i-2}$, $\Delta\tau_{i-1}$, $\Delta\tau_i$, and $\Delta\tau_{i+1}$, respectively. Meanwhile, the value of n_M is set with 4 for the grid node N_4 since it simultaneously holds partial probability amount of four adjacent grids g_{1-4}. With uniform velocity segmentation in both radial and azimuthal directions, the grid probability amount is directly dependent on the mesh resolution of the velocity grids.

Since the above procedure neglects the electron transit time of the velocity pairs nearby the grid center, there will probably be erroneous assignment of partial probability amount of the velocity grid. However, the grid probability amount and the above calculation error are inversely proportional to the total grid number, whose increment accordingly decreases the efficiency for calculating the detailed distribution of the electron transit time. To avoid unnecessary loss of calculation efficiency, the calculation accuracy can be optimized by repeatedly interpolating new velocity pairs into the discrete velocity grids after the initial mesh with a small number of velocity grids. As shown in Fig. 2(b), new interpolated velocities $u_r^{j,1}$ and $u_\phi^{k,1}$ at the probability midpoints of both directions ultimately form five velocity pairs at the edge midpoints and/or the center of each velocity grids, and the original grid is consequently split into four new adjacent grids. Note if the probability assignment is only distinguished in one direction, then it possibly only requires interpolating two new velocity pairs, such as the yellow-highlighted velocity grid in Fig. 2(b) resulting from the interpolation of $u_r^{j,1}$. In this case, the grid number can be significantly decreased compared to the uniform-mesh case without new velocity interpolations.

After sufficient velocity interpolations, the calculation of $G(\tau_i|\varphi_s)$ is fulfilled with the numerical method introduced in Ref. 31 and then expressed as

$$G(\tau_i|\varphi_s) = \sum_{l \in L}^{n_L} p_l / h, \tag{8}$$

where L and n_L are the index collection, and the total number of the grid nodes whose transit time is involved within the time interval $\Delta\tau_i$, and h refers to the identical width of the time intervals. Correspondingly, the population density of secondary electrons $K(\tau_i|\varphi_s)$ (see Table I for more details) can be further obtained in accordance with the calculation of the incident secondary emission yield (SEY), yielding

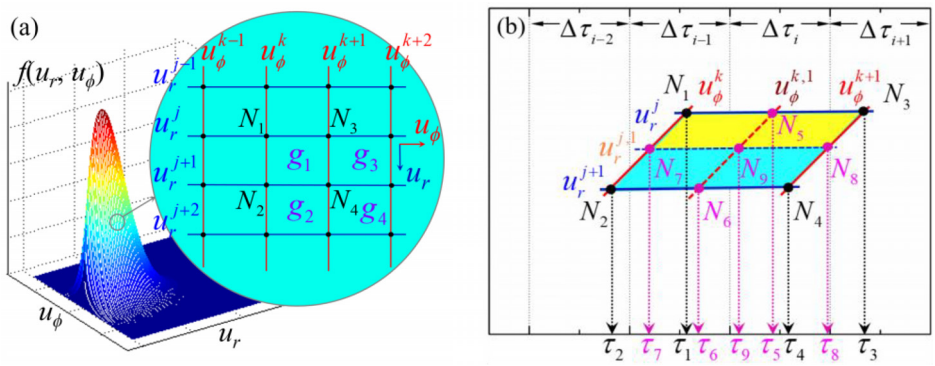

FIG. 2. The probability assignment scheme with the 2D randomness distribution of secondary emission velocity (a) and further optimization scheme with new velocity interpolation (b). The light-blue area in (a) zooms out the velocity grids delimited by the uniform velocity segmentations in both radial (blue solid) and azimuthal (red solid) directions. The original velocity grid g_1 is split into four small ones after interpolating new velocities in both radial and azimuthal directions. The yellow-highlighted velocity grid is formed by interpolating new velocity $u_r^{j,1}$ in the radial direction.

$$K(\tau_i|\varphi_s) = \sum_{l\in L}^{n_L} p_l \sigma(E_l, \theta_l)/h, \tag{9}$$

where $\sigma(E, \theta)$ is the empirical formula of SEY for the surface material, while the input parameters E_l and θ_l in Eq. (9) are the impact energy and angle corresponding to the velocity pair at the grid node N_l, yielding,

$$E = m_e\left(\upsilon_{ir}^2 + \upsilon_{i\phi}^2 + \upsilon_{iz}^2\right)/2, \tag{10}$$

$$\theta = \tan^{-1}\sqrt{\upsilon_{i\phi}^2 + \upsilon_{iz}^2}/\upsilon_{ir}, \tag{11}$$

where υ_{ir}, $\upsilon_{i\phi}$, and υ_{iz} are separately the velocity components in the radial, azimuthal, and axial direction at electron impacts, see Fig. 1 for more detailed illustration. Note that the following statistical calculation is mainly based on Furman's SEY formula, while Vaughan's SEY formula is also adopted in the following threshold analysis of the coaxial multipactor for comparison.

Meanwhile, the related parameters of electron transition and impact (including the impact type) are all obtained from electron trajectories, which can be calculated through numerically tracking electron motions or with the analytical trajectory equation approximately derived with the perturbation method.[30] For multipactor in the coaxial lines operated with the TEM mode, the numerical calculation of electron motions in the above algorithm is fulfilled upon the following differential equations:

$$\ddot{r} = -\frac{q_e}{m_e}\left[E_r(r,\phi,t) - \dot{z}B_\phi(r,\phi,t)\right] + r\dot{\phi}^2, \tag{12}$$

$$r\ddot{\phi} = -2\dot{r}\dot{\phi}, \tag{13}$$

$$\ddot{z} = -\frac{q_e}{m_e}\dot{r}B_\phi(r,\phi,t), \tag{14}$$

where q_e is the unit electron charge. Note again that it still needs to solve electron motions in the axial direction with the axial emission velocity set constant at zero although the 2D distribution function in Eq. (5) is adopted for electron emission randomness in the 1D3V modeling. Meanwhile, the calculation of Eq. (13) for trajectory tracking can be simplified according to the conservation of electron angular momentum. Without specification, the statistical analysis below is based on the numerical solution of electron motions for better accuracy.

C. Transit time distribution and related probability analysis

The JPDF construction in the 1D3V model developed above provides the requisite approach for the calculation of $G(\tau|\varphi_s)$ with both angular emission and impact of secondary electrons considered. The effect of angular momentum on the electron transition and related secondary electron population can be investigated through the comparison with the 1D1V result developed previously.

Figure 3 plots the probability distributions of electron transit time obtained with the 1D3V and 1D1V modeling separately for both the DS and SS impacts which are engendered by electron emissions from outer and inner conductor surface with the deterministic emission phase ($\varphi_s = 0.66\pi$). It shows that the probability transfer of secondary emission randomness from the radial velocity to the

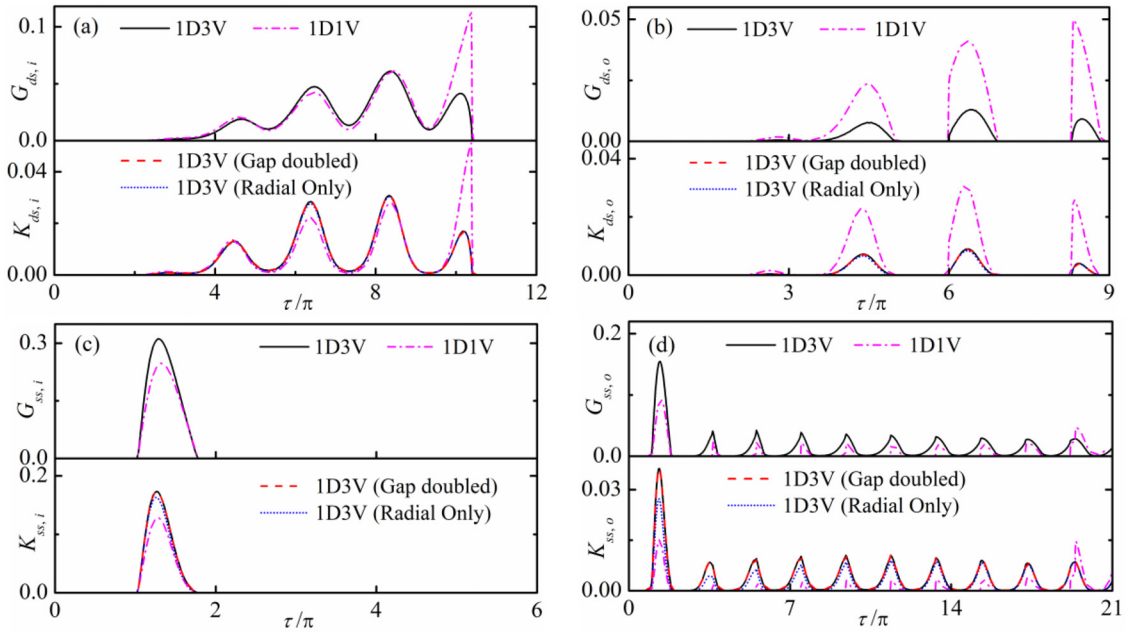

FIG. 3. Probability distribution of electron transit time obtained from the 1D3V (black solid) and 1D1V (purple dashed-dotted) modeling, respectively, for the double-sided (a) and (b) and single-sided (c) and (d) impacts of electrons emitted from inner (a) and (c) and outer (b) and (d) conductor surface in the coaxial multipactor with $R_o = 3.55$ mm, $R_i = 1.54$ mm, and $d = 2.01$ mm. The bottom subplots provide related population density of secondary electron with comparison to the 1D3V result which only considers the radial component of the electron impact energy (blue dotted) and the 1D3V result with the gap d increased up to 4.02 mm when γ and fd are kept constant (red dashed). The field parameters are $f = 1.64$ GHz, $V_{rf} = 120$ V, and $\varphi_s = 0.66\ \pi$, and the SEY constants of ECSS Ag are $E_1 = 30$ eV, $E_m = 165$ eV, and $\sigma_m = 2.22$.

azimuthal part apparently results in less DS impacts and more SS impacts since electron transitions are mainly determined by the radial motions. Meanwhile, we also see the same upper limit of the distribution range in the 1D1V and 1D3V results, which reveals the negligible effect of electron azimuthal motion on the transition condition from the SS impacts to the DS impacts. However, the centripetal term on the right side of Eq. (12) reveals the inevitable effect of the azimuthal motion on electron transitions in the 1D3V modeling, especially for SS impacts with relatively small radial velocity. As for the probability of SS impacts in the outer-emission case, it can be seen from the top subplot of Fig. 3(d) that the peaks in the middle region obtained from the 1D3V modeling are appreciably wider than the 1D1V result. This indicates that the azimuthal motion of electrons can produce notable variation in the transit time for the long-term SS impacts of the outer-emission events, where the transit time is sufficiently long to generate a remarkable difference in the radial motions when the corresponding emission velocity of electrons in the radial direction is close to its azimuthal counterpart.

Moreover, the bottom subplots in each part of Fig. 3 also compare the population density of secondary electrons [the calculation result of $K(\tau|\varphi_s)$] obtained from the 1D1V and 1D3V modeling. Note that the 1D3V result neglecting the azimuthal component of the electron impact energy (blue dotted line) is also included here for comparatively analyzing the contribution of angular momentum to secondary electron emissions. It can be seen that the incident SEY of the DS and SS impacts are both smaller than unity with the applied voltage below the breakdown level, and the former SEY is about twice as much as the latter according to the magnitude of $K(\tau|\varphi_s)$ and $G(\tau|\varphi_s)$. As for the low peaks illustrated in the bottom subplot of Fig. 3(d), the value of $K_{ss,o}$ increases with the increment of the transit time as opposed to the downtrend of $G_{ss,o}$, for the long transit time of electrons is mainly caused by higher radial emission velocity which correspondingly leads to larger kinetic energy from the field acceleration. Accordingly, the notable difference between the results of $K_{ss,o}$ regarding and disregarding angular momentum diminishes with the increasing transit time for the SS impacts or even turns insignificant after their transition to DS impacts. On the other hand, there is no variation in the 1D3V results of $K(\tau|\varphi_s)$ when the gap d of the coaxial lines is increased from 2.01 mm to 4.02 mm with γ and fd (product of f and d) kept constant. It proves the validity of the fd scaling law of multipactor threshold in the 1D3V result based on the direct dependence of the effective SEY on the result of $K(\tau|\varphi_s)$ detailed in Subsection II D.

Meanwhile, the overall probability of electron impacts $P(\varphi_s)$ and the overall population of secondary electron $S(\varphi_s)$ (see the detailed definitions in Table I) can be obtained with the following integrals of $G(\tau|\varphi_s)$ and $K(\tau|\varphi_s)$, having

$$P(\varphi_s) = \int_0^\infty G(\tau|\varphi_s)d\tau, \tag{15}$$

$$S(\varphi_s) = \int_0^\infty K(\tau|\varphi_s)d\tau. \tag{16}$$

Accordingly, the ratio of $P(\varphi_s)$ and $S(\varphi_s)$ is denoted as $\delta(\varphi_s)$, which essentially accounts for the mean SEY of electron impacts for angular electron emissions with deterministic phase φ_s. It is used to analyze the SEY variation caused by angular impacts with different emission phases. On that basis, the calculation results of $P(\varphi_s)$, $S(\varphi_s)$, and $\delta(\varphi_s)$ obtained with the 1D3V and 1D1V modeling for different emission phases are plotted in Fig. 4 for further comparison. As can be seen, the 1D3V and 1D1V results of $P(\varphi_s)$ with remarkable magnitude discrepancy manifest same varying pattern in accordance with the favorability of electron transitions on the emission phase. Especially, for the inner-emission cases, the outwards acceleration effect eventually results in no SS impacts for the emission phases within the range of $[0, \pi/2]$ and further leads to apparent distribution asymmetry. In the meantime, significant SEY increment of both the DS and SS impacts is commonly evinced for the consideration of the impact angle, which reveals more population of secondary electron in the 1D3V modeling as well. However, it is still possible to find slight SEY decrement in the DS impacts with the electron emission phases around 0 or 2π, where more SEY variation is caused by the kinetic energy loss with relatively small emission velocity in the radial direction. Meanwhile, the probability transfer from DS impacts to SS impacts can also be observed for the whole distribution of the electron emission phase in the 1D3V results. The resultant probability decrease of the DS impacts accordingly reduces the population of secondary electron since the DS impacts with dominant contribution to multipactor formation can

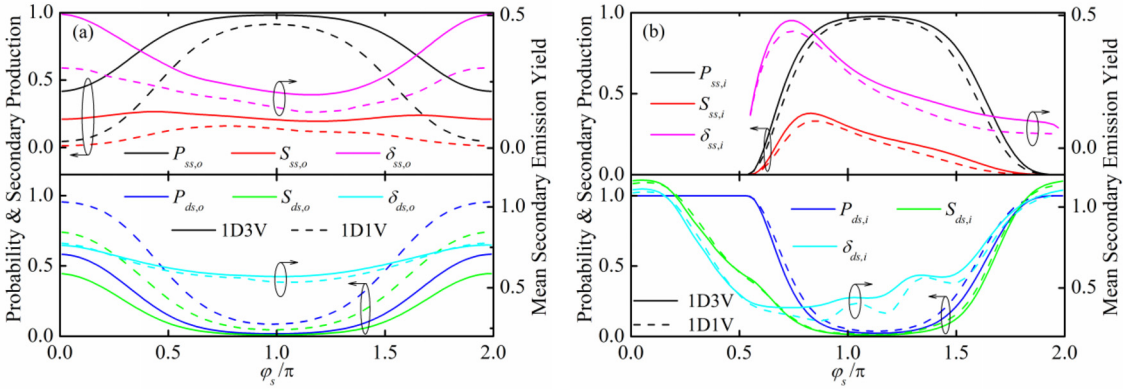

FIG. 4. The overall transition probability $P(\varphi_s)$ and the overall population of secondary electron $S(\varphi_s)$ as well as the mean secondary emission yield $\delta(\varphi_s)$ obtained with the 1D3V (solid line) and 1D1V (dashed line) modeling for electron impacts in the outer-emission (a) and inner-emission (b) cases with different emission phases. The parameter setting is the same with Fig. 3.

obtain higher kinetic energy from sufficient field acceleration in contrast to the SS impacts. Regarding the potential effect of the varying radius ratio on the SEY variation for angular impacts in the coaxial multipactor, there is still a need to further evaluate the above contrary effect of angular momentum on multipactor threshold determination.

D. Process description of the coaxial multipactor

As mentioned previously, angular spatial transport of multipactor electrons is neglected due to the azimuthal symmetry of multipactor development in the coaxial lines. Therefore, this 1D3V modeling still adopts the previous 1D statistical description for the multipactor formation process in the coaxial lines based on the numerical construction algorithm of the JPDF developed above. To analyze the distribution characteristics of the impact energy and angle, nonstationary statistical formulation of the coaxial multipactor with further investigation into its mechanism is detailed below for completeness.

As the prerequisite definitions, the electron emission and impact rates at the incident field phase φ (electrons/radian) during multipactor formation in the coaxial lines are separately denoted with $C(\varphi)$ and $I(\varphi)$, and the corresponding subscripts "o" and "i" are used to differentiate these rate parameters with different emissions from the outer and inner conductor, respectively. Regarding the mutual contributions of the DS and SS impacts, the electron emission rates at the inner and outer surface can be expressed in combination with Eq. (9), yielding

$$C_o(\varphi) = \int_0^{\varphi} C_i(\varphi_s) K_{ds,i}(\varphi - \varphi_s|\varphi_s) d\varphi_s + \int_0^{\varphi} C_o(\varphi_s) K_{ss,o}(\varphi - \varphi_s|\varphi_s) d\varphi_s + \psi_o(\varphi), \tag{17}$$

and

$$C_i(\varphi) = \int_0^{\varphi} C_o(\varphi_s) K_{ds,o}(\varphi - \varphi_s|\varphi_s) d\varphi_s + \int_0^{\varphi} C_i(\varphi_s) K_{ss,i}(\varphi - \varphi_s|\varphi_s) d\varphi_s + \psi_i(\varphi), \tag{18}$$

where $\psi_o(\varphi)$ and $\psi_i(\varphi)$ represent the secondary electron emissions from external sources on the outer and inner surface separately, having $\tau = \varphi - \varphi_s$.

Likewise, electron impact rates on either surface can be expressed analogously in combination to Eq. (8) as

$$I_o(\varphi) = \int_0^{\varphi} C_i(\varphi_s) G_{ds,i}(\varphi - \varphi_s|\varphi_s) d\varphi_s + \int_0^{\varphi} C_o(\varphi_s) G_{ss,o}(\varphi - \varphi_s|\varphi_s) d\varphi_s, \tag{19}$$

and

$$I_i(\varphi) = \int_0^{\varphi} C_o(\varphi_s) G_{ds,o}(\varphi - \varphi_s|\varphi_s) d\varphi_s + \int_0^{\varphi} C_i(\varphi_s) G_{ss,i}(\varphi - \varphi_s|\varphi_s) d\varphi_s. \tag{20}$$

On that basis, the total electron emissions inside the gap can be obtained with the difference of $C(\varphi)$ and $I(\varphi)$, thus

$$N(\varphi) = \int_0^{\varphi} C_o(\varphi') - I_o(\varphi') d\varphi' + \int_0^{\varphi} C_i(\varphi') - I_i(\varphi') d\varphi'. \tag{21}$$

Meanwhile, the ratio of $C(\varphi)$ and $I(\varphi)$ also accounts for the instantaneous SEY at electron impacts in the multipactor dynamics. For the sake of convenience in multipactor threshold determination, the following effective SEY σ_{eff} is further introduced to quantify the variation tendency of electron population, which essentially represents the multipactor severity

$$\sigma_{eff} = \frac{\int_{\varphi_t}^{\varphi} (C_o(\varphi') + C_i(\varphi')) d\varphi'}{\int_{\varphi_t}^{\varphi} (I_o(\varphi') + I_i(\varphi')) d\varphi'}. \tag{22}$$

Note that the time window $[\varphi_t, \varphi]$ is commonly set in the steady-state stage of multipactor evolution. It is apparent that multipactor breakdown takes place when σ_{eff} is larger than unity, and the multipactor onset condition can be determined with $\sigma_{eff} = 1$ for multipactor threshold calculation or full susceptibility chart. Note that the initial seeding is necessary for the process modeling of electron multiplication, but its effect is negligible in determining the calculation result of σ_{eff}. Hence, the injection of the seeding electrons is assumed at $\varphi = 0$ with same amount on the outer and inner surface. Meanwhile, the discrepancy between the threshold determination using nonstationary and stationary formulation is negligible as revealed in Ref. 17.

Along with the dynamic modeling, further analysis of coaxial multipactor mechanism can be conducted through the statistical count on the electron impact energy and angle during the multipactor process. As illustrated in Eqs. (8) and (9), the specific values of $G(\tau|\varphi_s)$ and $K(\tau|\varphi_s)$ in the 1D3V algorithm are determined by the probability amount of the involved velocity grid nodes. It is worth emphasizing that one probably needs to count different electron impact energies and angles for the specified parameters φ_s and τ since there are usually more than one velocity grid nodes involved. As for the involved lth grid node, the impact energy $E_l(\tau|\varphi_s)$ and the impact angle $\theta_l(\tau|\varphi_s)$ of secondary electrons can be calculated along with the electron transit time using Eqs. (10) and (11) when numerically tracking electron trajectories, and the corresponding weight of electron number $w_l(\tau|\varphi_s)$ can be written as

$$w_l(\tau|\varphi_s) = p_l(\tau|\varphi_s) C(\varphi_s). \tag{23}$$

With the above derivations, the distribution of the impact energy $D(E)$ and the impact angle $D(\theta)$ during multipactor formation can be obtained through collecting all the weight data of electron impacts within several RF periods in the steady state $[\varphi_t, \varphi]$ and performing related statistics and normalization. Note the subscripts "o," "i," and "t" are used below to differentiate the distributions for electron impacts at the outer surface, the inner surface, and both surfaces, respectively. Moreover, the overall average of the impact energy E_m and the impact angle θ_m can be calculated with

$$E_m = \frac{\int_{\varphi_t}^{\varphi} \int_0^{\varphi'} \sum_l^{n_L(\varphi_s,\varphi')} E_l(\varphi' - \varphi_s|\varphi_s) w_l(\varphi' - \varphi_s|\varphi_s) d\varphi_s d\varphi'}{\int_{\varphi_t}^{\varphi} \int_0^{\varphi'} \sum_l^{n_L(\varphi_s,\varphi')} w_l(\varphi' - \varphi_s|\varphi_s) d\varphi_s d\varphi'}, \tag{24}$$

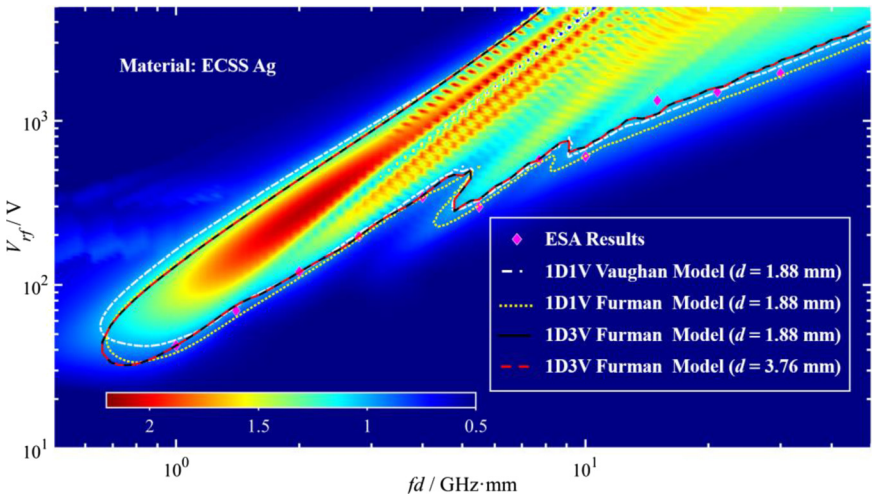

FIG. 5. Multipactor susceptibility chart with the 1D3V and 1D1V statistical modeling for 50 Ω coaxial lines (R_o = 3.33 mm, R_i = 1.45 mm, and d = 1.88 mm) with ECSS Ag coating. Multipactor curves determined by the 1D1V statistical modeling using the modified Vaughan's formula (white dotted-dashed) and Furman's formula (yellow dotted) as well as the 1D3V statistical modeling with d = 1.88 mm (black solid) and d = 3.76 mm (red dashed) are plotted with the threshold results (purple diamond) from ESA for comparison.

$$\theta_m = \frac{\int_{\varphi_t}^{\varphi}\int_0^{\varphi'}\sum_l^{n_L(\varphi_s,\varphi')}\theta_l(\varphi'-\varphi_s|\varphi_s)w_l(\varphi'-\varphi_s|\varphi_s)d\varphi_s d\varphi'}{\int_{\varphi_t}^{\varphi}\int_0^{\varphi'}\sum_l^{n_L(\varphi_s,\varphi')}w_l(\varphi'-\varphi_s|\varphi_s)d\varphi_s d\varphi'}, \quad (25)$$

where n_L is the total number of the grid nodes where the corresponding transit time of electrons are involved within the time interval of $\varphi'-\varphi_s$ for electron emissions at the specified phase φ_s.

III. RESULTS AND ANALYSIS

With the implementation optimization elaborated above, the 1D3V statistical modeling of multipactor is hereby fulfilled for multipactor threshold calculation through numerically tracking electron trajectories with both angular emissions and impacts of multipactor electrons considered. This optimization inherently enables multipactor statistical modeling to disregard the field complexity and better match the physical process of secondary electron emissions, which accordingly leads to better accuracy and feasibility in the threshold calculation and mechanism analysis for multipactor in the coaxial lines with any radius ratio. Thereupon, this section further quantitatively investigates the underlying effect of electron angular momentum on the multipactor formation of coaxial lines through calculating and comparing multipactor threshold and related impact angle distribution for the coaxial multipactor with different radius ratios.

As a preliminary verification of calculation accuracy, the multipactor susceptibility zone of typical 50 Ω coaxial lines coated with ECSS (European Cooperation for Space Standardization) Ag is charted with the 1D1V and 1D3V modeling and plotted in Fig. 5. The susceptibility chart is fulfilled through calculating σ_{eff} for the array parameters with a uniform resolution of 135 × 100. Moreover, the multipactor threshold results at typical frequency points from ESA (European Space Agency)[36] are also plotted in Fig. 5 for comparative analysis. For consistency, the multipactor threshold results are obtained in company with the SEY measurement of the experimental samples, see more details with the measurement error in Ref. 37. In accordance with the ESA results, the following geometric parameters adopted for the statistical modeling are set with R_o = 3.33 mm, R_i = 1.45 mm, and d = 1.88 mm, and the parameters of the SEY formula are fitted to the measured SEY constants of ECSS Ag (the crossover energies $E_{1/2}$, the SEY maximum σ_{max}, and its corresponding energy E_{max}). As revealed from the probability analysis in Sec. II, angular SS impacts with low kinetic energy are more likely to produce more secondary electron emissions for relatively larger impact angles, and the SEY variance of angular impacts in Vaughan's formula is neglected when the kinetic energy is lower than the threshold energy. For this reason, Vaughan's formula adopted in the previous 1D1V modeling is replaced here with Furman's formula, see Refs. 30 and 33 for the formula details and Table II for the related parameter setting. Note that the parameter value of k_{2-5} in Vaughan's formula for determining the upper susceptibility boundary is modified according to the experimental data of the second-crossover energy (E_2 = 5000 eV). Furthermore, the parameter value of Furman's formula is extracted from the commercial software CST Particle studio, which is also used for providing the simulation result of CST in Table III.

In contrast to Vaughan's formula, the slightly higher SEY value in Furman's formula caused by curve-fitting leads to relatively lower multipactor threshold, see the calculation error listed in Table III for

TABLE II. Parameters of Furman's formula and the modified Vaughan's formula.

$P_{1,e}(\infty)$	$\hat{P}_{1,e}$	$\hat{E}_e$	w	p	e_1	e_2	$P_{1,r}(\infty)$	E_r	r	r_1	r_2
0.02	0.05	0.0	60.86	1.0	0.26	2.0	0.01	0.041	0.104	0.26	2.0
$\hat{\delta}_{ts}$	$\hat{E}_{ts}$	s	t_1	t_2	t_3	t_4	k_1	k_2	k_3	k_4	k_5
2.22	165	1.32	0.66	0.80	0.70	1.00	0.56	0.125	1.22	0.28	3.5

TABLE III. Calculation error of multipactor threshold obtained with different statistical modeling and CST simulation[a].

	Calculation error of multipactor threshold (dB)			
fd (GHz mm)	1D1V Vaughan	1D1V Furman	1D3V Furman	CST Furman
1.0	0.686	−0.879	−0.103	−2.174
1.4	0.593	−0.799	0.510	−1.642
2.0	−0.146	−0.730	−0.301	−1.082
2.8	0.607	−0.279	0.097	−0.514
4.0	0.829	−0.046	0.263	−1.035
5.5	0.832	0.136	1.066	0.226
7.7	0.155	−0.479	0.242	−1.789
10.0	0.892	0.145	1.144	−0.274
15.0	−1.846	−3.076	−1.546	−3.083
21.0	0.019	−1.176	0.553	0.199
30.0	0.958	−0.348	1.432	0.965

[a]ESA threshold data from ECSS document.[36]

more details on the 1D1V result comparison. Nonetheless, the 1D3V Furman model also can achieve fairly good agreement with the ESA results similar to the previous 1D1V Vaughan model. To be specific, the average calculation errors of multipactor threshold from the 1D3V and 1D1V modeling are 0.66 dB and 0.69 dB, respectively. At the cost of tolerable accuracy loss of multipactor threshold calculation at high frequencies, the 1D3V modeling is able to obtain relatively better accuracy at low-frequency points. Especially for the leftmost frequency point, the calculation accuracy of multipactor threshold at $fd = 1.0\,\text{GHz}\cdot\text{mm}$ can be improved by as much as 0.58 dB with the 1D3V Furman model. Meanwhile, the calculation accuracy for $fd = 2.8\text{GHz}\cdot\text{mm}$ and $fd = 4.0\,\text{GHz}\cdot\text{mm}$ are decreased to 0.1 dB and 0.26 dB, respectively, which proves the capability of the 1D3V modeling for accurate threshold calculation of first multipactor orders. Conversely, the average accuracy loss of multipactor threshold calculation at high-frequency points is around 0.22 dB, whereas the accuracy at $fd = 15\,\text{GHz}\cdot\text{mm}$ can still be improved by 0.3 dB instead. It also shows in Fig. 5 that multipactor threshold voltages obtained with the 1D3V modeling are apparently larger than the 1D1V result when adopting Furman's formula. This convincingly reveals the more significant effect of the probability transfer from DS impacts to SS impacts on the threshold determination in contrast to the SEY increment caused by angular impacts of secondary electrons in the coaxial multipactor, which, thus, leads to significant increment of multipactor threshold in the 1D3V result. Also, it shows from Table III that CST simulations with Furman's SEY formula tend to obtain smaller multipactor threshold voltage for most frequencies than the 1D3V statistical modeling, which is possibly attributed to the different distribution of secondary emission randomness adopted.

Meanwhile, the overlapped multipactor curves of 50 Ω coaxial lines with different gap ($d = 1.88$ mm and $d = 3.76$ mm) in the threshold results of Fig. 5 prove that the *fd* scaling law of multipactor threshold stands in the 1D1V modeling as well as the 1D3V modeling with electron angular momentum included, which is consistent with the parameter normalization and the probability analysis in Sec. II. Thus, we can also conclude that the impact angle of multipactor electrons in the coaxial lines is independent of the surface curvature according to its correlation with the radius ratio γ and the gap d as shown in the Appendix. Likewise, same threshold result can be obtained for the geometric parameters of $R_o = 3.55$ mm, $R_i = 1.54$ mm, and $d = 2.01$ mm, which is adopted in the above probability analysis as well as the following mechanism analysis.

To give a comprehensible view of the electron impact angle for the coaxial multipactor, the impact angle distributions at different surfaces are calculated for different RF voltage cases at the specified frequency of 1.15 GHz using the 1D3V Furman model, see Fig. 6 for more details. This distribution analysis is conducted at the specified frequency of 1.15 GHz in view of excellent calculation accuracy of multipactor threshold at the adjacent frequency points mentioned above. As can be seen, the nonuniform distribution density of the impact angle of multipactor electrons at the outer surface D_o, the inner surface D_i, and both surfaces D_t [see the definitions in Eq. (23)] all generally decrease vs the impact angle, and most impact angles are concentrated in the range of [0°, 30°]. However, the average impact angle at the inner surface is larger than that at the outer surface viewing from the relatively higher magnitude of D_i in the angle range of [15°, 30°]. This difference is caused by the opposite effect of the Miller (or pondermotive) force[38] on the impact angle of electron impacts on the inner and outer conductor surface as explained in Sec. II. It needs interpretations that the Miller force is the outwards-pushing force caused by the potential gradient of the high-frequency field.

Furthermore, the distribution of D_t is close to that of D_o for the dominant contribution of electron impacts at the outer surface to multipactor formation in the 50 Ω coaxial lines. Meanwhile, the impact angle distribution is shifted and concentrated to the range of [0°, 10°] with increasing RF voltage, and the average impact angles for the RF voltage at the below-breakdown, threshold-breakdown, and above-breakdown conditions are 20°, 15°, and 13°, respectively. This decrease of the average impact angle with increasing RF voltage is attributed to higher radial kinetic energy of the DS impacts from the field acceleration with higher RF voltage. This can also be used to explain relatively larger threshold difference of the high-order multipactor between the 1D1V and 1D3V results as shown in Fig. 5, for higher threshold voltage of high frequencies results in smaller impact angle of angular impacts, which accordingly leads to less SEY increment and larger threshold increment in the 1D3V results.

According to the above analysis, the impact angle of multipactor electrons is independent of the curvature of the conductor surface but highly sensitive to the applied RF voltage in the coaxial lines. To evaluate the influence of the device geometry and angular momentum on multipactor formation, the 1D1V and 1D3V models are further adopted here to calculate the multipactor threshold voltage of the coaxial lines with different radius ratio γ, see Fig. 7 for more details. The threshold analysis is performed at the specified frequency points of 1.15 GHz and 3.0 GHz to cover different multipactor orders according to different-order multipactor zones at $fd = 2.31\,\text{GHz}\cdot\text{mm}$ and $fd = 6.03\,\text{GHz}\cdot\text{mm}$ charted in Fig. 5, see the definition of multipactor order in Ref. 22. Meanwhile, the gap between the inner and outer conductor of coaxial lines is kept constant at 2.01 mm with γ varying in the range of [1.0, 4.0]. Actually, the coaxial lines with the radius ratio equal to unity turn into two infinite parallel plates, so the quantitative analysis above is also intended to answer the question "How does

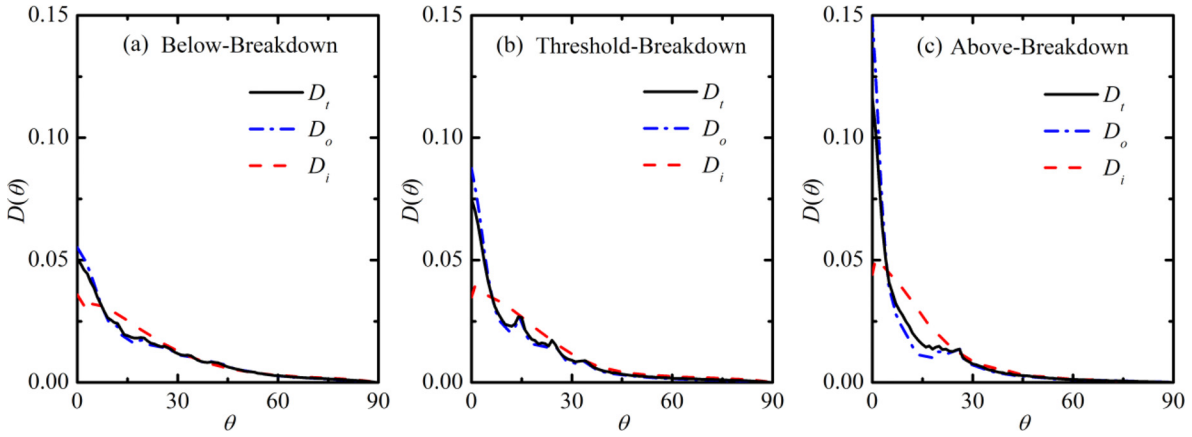

FIG. 6. Impact angle distribution of electron impacts on the outer surface D_o (blue dashed-dotted), the inner surface D_i (red dashed), and both surfaces D_t (black solid) in multipactor of the coaxial lines obtained with the 1D3V modeling for the below-breakdown case with $V_{rf} = 100$ V (a), the threshold-breakdown case with $V_{rf} = 140$ V (b), and the above-breakdown case with $V_{rf} = 200$ V (c). The other parameters are $R_o = 3.55$ mm, $R_i = 1.54$ mm, $d = 2.01$ mm, and $f = 1.15$ GHz.

multipactor threshold voltage vary when two semi-infinite parallel plates are bent into coaxial lines?" posed at the beginning of this paper. In Fig. 7, we observe sudden rise of the multipactor threshold in the 1D1V and 1D3V results for γ located in [2.6, 2.8] which is caused by the discrete order shift of the coaxial multipactor with the increase of the radius ratio, see more related explanation in Ref. 17. Furthermore, the threshold voltage with slight magnitude discrepancy between the 1D1V and 1D3V results exhibits a monotonous decrease when the radius ratio is marginally increased from unity. However, in contrast to the nearly monotonous variation in the 1D1V result before the sudden rise, the threshold voltages for the first-order ($f = 1.15$ GHz) and high-order ($f = 3.0$ GHz) multipactor in the 1D3V results both reach their minimum when γ increases up to 2.1 and 1.4 separately. Moreover, the threshold difference between the 1D1V and 1D3V results for the high-order multipactor turns more significant with the sudden rise of threshold voltage at different value of γ, which accordingly reveals more significant effects of angular emissions and impacts on the high-order multipactor.

To illustrate the underlying mechanism for the above varying pattern of multipactor threshold vs the radius ratio, the average impact angle of different surfaces at the threshold-multipactor voltage is calculated with the 1D3V model for the specified frequency of 1.15 GHz, see more details in Fig. 8. Besides the ratio of the average impact rates at the outer and inner surface, I_o/I_i is also provided here for better demonstration. It can be seen that $\theta_{m,o}$ and $\theta_{m,i}$ vary in the opposite way vs γ in the whole distribution for the contrary contribution of the Miller force to the variation of the average impact angle on the outer and inner surface as discussed above. Furthermore, there is an increasing similarity between the varying patterns of $\theta_{m,o}$ and $\theta_{m,t}$, especially for the single-surface multipactor with higher radius ratio when I_o/I_i exceeds an order of magnitude.

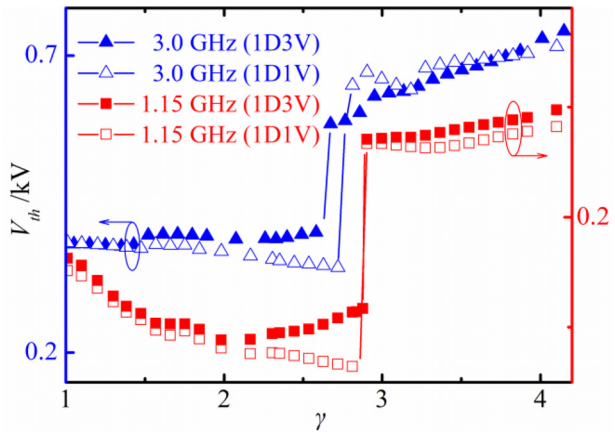

FIG. 7. Multipactor threshold voltage of the coaxial lines ($d = 2.01$ mm) vs the radius ratio obtained with the 1D1V (hollow) and 1D3V (solid) model for the specified frequencies of 1.15 GHz (red rectangle) and 3.0 GHz (blue triangle).

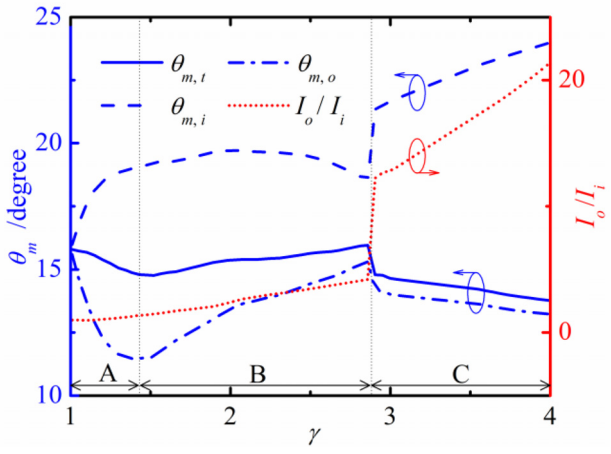

FIG. 8. The average impact angle at outer surface $\theta_{m,o}$ (blue dashed-dotted), inner surface $\theta_{m,i}$ (blue dashed), and both surfaces $\theta_{m,t}$ (blue solid) vs the radius ratio for the specified frequency of 1.15 GHz as well as the ratio of the average impact rates at the outer and inner surface I_o/I_i (red dotted) with $d = 2.01$ mm.

In general, the whole distribution of the average impact angle is divided into three primary sections with different varying pattern. For section A, the asymmetry of the inner and outer multipactor developments in the coaxial lines remains insignificant when the radius ratio is close to unity, so the coaxial multipactor is still established by the mutual contribution of the SS and DS impacts. However, the field nonuniformity is gradually exacerbated with the increase of the radius ratio, see the increasing difference between the field amplitude at the inner and outer surface in Fig. 9. The Miller force tends to produce more kinetic acceleration to electron impacts on the outer surface and, thus, engender sharp decrement in $\theta_{m,o}$ which is mostly contributed by the higher-energy DS impacts. When γ is located in section B, $\theta_{m,o}$ increases for the gradual deduction of the above angle increment contributed by the DS impacts. This is because the proportion of the DS impacts in the coaxial multipactor greatly reduces when the field nonuniformity becomes significant with the increasing radius ratio. In these two sections, multipactor threshold variation is primarily governed by the increment of the impact angle at the inner surface since the contributions from the increasing impact energy and the decreasing impact angle at the outer surface are almost compensated for secondary electron production. As for section C, the smooth decrease of $\theta_{m,o}$ is merely caused by the further increment of the impact angle of SS impacts at the outer surface, for there is almost no DS impacts in the coaxial multipactor with high I_o/I_i after the sudden rise of the multipactor threshold voltage.

As final discussion, the consideration of electron angular momentum in the 1D3V statistical modeling inevitably leads to tracking more electron trajectories, which is, indeed, at the cost of further calculation efficiency. The adoption of an approximate trajectory equation is helpful for improving the efficiency of full multipactor susceptibility chart, but the resulting calculation error is depending on the approximation validity of analytical trajectory equation. However, the efficiency optimization algorithm by reutilizing electron trajectories is also available for multipactor susceptibility chart with different coating materials since the JDPF construction is independent of the SEY evaluation in this 1D3V statistical modeling as well.

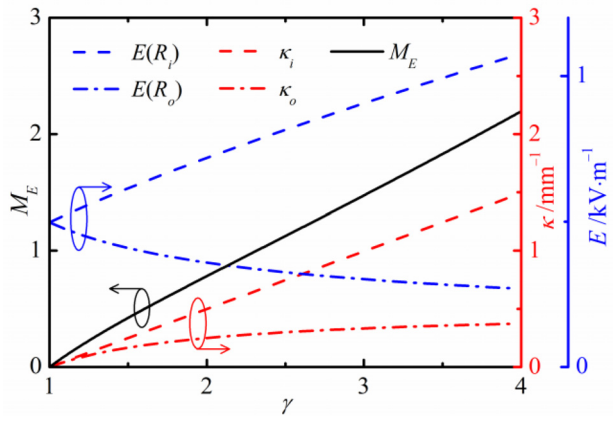

FIG. 9. Illustration for the magnitude parameter (black solid) vs the radius ratio with the inner (red dashed) and outer (red dashed-dotted) surface curvature and the field amplitude at the inner (blue dashed) and outer (blue dashed-dotted) conductor surface. The main parameters are $d = 2.01$ mm and $V_{rf} = 1$ V.

Meanwhile, this 1D3V statistical modeling is appropriate for investigating multipactor breakdown in coaxial lines with any radius ratio as well as multipactor cases where the proportion and the impact angle of electron angular impact are possibly increased for the induced external field (i.e., multipactor in the parallel plates or the coaxial lines with transverse electrostatic field or vertical magnetostatic field) or the existence of the curved surface (i.e., multipactor in the circular waveguide). With further development, the above modeling method can be further extended for the 2D3V multipactor statistical model regarding the spatial transport of electron population at different positions.

IV. CONCLUSIONS

In this paper, the effect of electron angular momentum on multipactor formation of the coaxial lines is investigated quantitatively through threshold analysis with the 1D3V multipactor statistical modeling, which takes both angular emissions and impacts of secondary electrons into account. This improved statistical modeling can disregard the field complexity and adequately match the real physical multipactor process with complete emission randomness and angular impacts of secondary electrons, which, thus, results in better accuracy and feasibility in multipactor threshold calculation and mechanism analysis. The result comparison indicates that the 1D3V statistical modeling with Furman's SEY formula can achieve fairly good agreement with the threshold results of ESA in contrast to previous 1D1V modeling. At the cost of tolerable accuracy loss at high frequencies, the calculation accuracy of multipactor threshold for low frequencies with the 1D3V modeling can be improved by 0.58 dB at best. Meanwhile, the analysis has revealed a more significant effect concerning the probability transfer from double-sided impacts to single-sided impacts on the multipactor threshold determination, compared to the SEY increment caused by the angular impacts in the coaxial multipactor.

The discrepancy of multipactor threshold variation between the 1D1V and 1D3V results reveals the growing significance of angular impacts of secondary electrons with the increasing radius ratio and its indispensable effect on multipactor formation in the coaxial lines. It was found that the 1D3V result of multipactor threshold voltage nonmonotonically varies with the radius ratio and reaches its minimum when the radius ratio increases up to 2.2 and 1.4 for the first-order (2.31 GHz · mm) and high-order (6.03 GHz · mm) multipactor separately. This is different from the nearly monotonous decrease in the 1D1V result and more significant discrepancy shows in the high-order multipactor. The mechanism analysis also reveals the outwards-pushing force caused by the field nonuniformity results in increasing and decreasing impact angle for the angular impacts on the inner and outer surface, respectively, and leads to the nonmonotonous variation of the average impact angle with the increasing radius ratio due to the associated proportion decrease of the double-sided impacts in the coaxial multipactor.

ACKNOWLEDGMENTS

This research was supported by the National Natural Science Foundation of China (Grant Nos. 61801370, U1537210, and 61971342). The MSU Team was supported by AFOSR MURI under Grant Nos. FA9550-18-1-0062 and FA9550-21-1-0367.

AUTHOR DECLARATIONS

Conflict of Interest

The authors have no conflicts to disclose.

Author Contributions

Shu Lin: Conceptualization (equal), Data curation (equal), Formal analysis (equal), Funding acquisition (equal), Investigation (equal), Methodology (equal), Project administration (equal), Resources (equal), Software (equal), Supervision (equal), Validation (equal), Visualization (equal), Writing – original draft (equal), and Writing – review & editing (equal). **Yongdong Li:** Funding acquisition (equal) and Supervision (equal). **Hao Qu:** Data curation (equal), Validation (equal), and Visualization (equal). **Patrick Wong:** Formal analysis (equal), Funding acquisition (equal), Validation (equal), and Writing – review & editing (equal). **Peng Zhang:** Formal analysis (equal), Funding acquisition (equal), and Writing – review & editing (equal). **John P. Verboncoeur:** Conceptualization (equal), Formal analysis (equal), Funding acquisition (equal), and Writing – review & editing (lead). **Huan Zhong:** Data curation (equal). **Yonggui Zhai:** Data curation (equal) and Software (equal). **Meng Cao:** Conceptualization (equal) and Funding acquisition (equal). **Hongguang Wang:** Conceptualization (equal) and Software (equal).

DATA AVAILABILITY

The data that support the findings of this study are available from the corresponding author upon reasonable request.

APPENDIX: THE SURFACE CURVATURE AND THE RESULTANT ACCELERATION EFFECT FOR ELECTRON MOTIONS IN COAXIAL LINES

The surface curvature is defined as the reciprocal of the radius for either conductor surface of the coaxial lines. When the gap d is kept constant, the correlation of the outer (κ_o) and inner (κ_i) surface curvature to the radius ratio γ is, respectively, expressed as

$$\kappa_o = \frac{1}{d}\left(1 - \frac{1}{\gamma}\right), \tag{A1}$$

$$\kappa_i = \frac{1}{d}(\gamma - 1). \tag{A2}$$

Apparently, κ_o and κ_i are both negatively correlated to d but positively correlated to γ as shown in Fig. 9, so they are both halved when d is doubled for the constant γ. The amplitude of the nonuniform field $E(r)$ and the resultant Miller force $\mathbf{F}(r)$ between the inner and outer conductor are separately expressed with

$$E(r) = \frac{V_{rf}}{r \ln \gamma}, \tag{A3}$$

$$\mathbf{F}(r) = F(r)\mathbf{e_r} = \frac{P_c d^3}{r^3 \ln^2 \gamma}\mathbf{e_r}, \tag{A4}$$

where $P_c = q_e{}^2 V_{rf}{}^2/2m_e\omega^2 d^3$. It reveals that the field non-uniformity in the coaxial lines increases vs the radial ratio from the difference of the field amplitude at the inner and outer conductor surface in Fig. 9. There also shows similar varying pattern in M_E which is the magnitude parameter defined for evaluating the equivalent Miller force and calculated with the following integral:

$$M_E = \frac{\int_{R_i}^{R_o} F(r)dr}{P_c d} = \frac{(\gamma^2 - 1)(\gamma - 1)^2}{\gamma^2 \ln^2 \gamma}. \tag{A5}$$

It shows in Fig. 9 that the outwards acceleration effect caused by the field nonuniformity is also exacerbated with the increasing radius ratio.

REFERENCES

[1] J. R. M. Vaughan, IEEE Trans. Electron Devices **35**(7), 1172 (1988).
[2] C. Jing, S. H. Gold, R. Fischer, and W. Gai, Appl. Phys. Lett. **108**(19), 193501 (2016).
[3] M. Jimenez, B. Martinez, D. Raboso, S. Anza, A. Alvarez, F. Quesada, V. E. Boria, C. Vicente, and J. Gil, IEEE Microwave Wireless Compon. Lett. **22**(2), 61 (2012).
[4] J. Vague, J. C. Melgarejo, M. Guglielmi, V. E. Boria, S. Anza, C. Vicente, R. Moreno, M. Taroncher, B. Gimeno, and D. Raboso, IEEE Trans. Microwave Theory Tech. **66**(8), 3644 (2018).
[5] P. Y. Wong, Y. Y. Lau, P. Zhang, N. Jordan, and J. Verboncoeur, Phys. Plasmas **26**(11), 112114 (2019).
[6] L. Zhang, Y. Li, S. Lin, H. Wang, C. Liu, J. Li, and Z. Xu, Phys. Plasmas **25**(8), 082301 (2018).
[7] R. Udiljak, D. Anderson, P. Ingvarson, U. Jordan, U. Jostell, L. Lapierre, G. Li, M. Lisak, J. Puech, and J. Sombrin, IEEE Trans. Plasma Sci. **31**(3), 396 (2003).
[8] S. Mori, M. Yoshida, and D. Satoh, Phys. Rev. Accel. Beams **24**(2), 022001 (2021).
[9] K. H. Jang, S. J. Wang, H. H. Wi, K. Saito, and J. G. Kwak, Fusion Eng. Des. **161**(2), 111960 (2020).
[10] C. Chang, Y. D. Li, J. Verboncoeur, Y. S. Liu, and C. L. Liu, Phys. Plasmas **24**(4), 040702 (2017).
[11] X. Qiu, M. A. Saed, J. J. Mankowski, J. Dickens, and R. P. Joshi, AIP Adv. **11**(2), 025039 (2021).
[12] I. Montero, L. Olano, L. Aguilera, M. Davila, U. Wochner, D. Raboso, and P. Martin-Iglesias, J. Electron Spectrosc. Relat. Phenom. **241**, 146822 (2019).
[13] Y. Li, M. Ye, Y. N. He, W. Z. Cui, and D. Wang, Phys. Plasmas **24**(11), 113505 (2017).
[14] A. Iqbal, P. Y. Wong, D. Q. Wen, S. Lin, J. Verboncoeur, and P. Zhang, Phys. Rev. E **102**(4), 043201 (2020).
[15] M. Siddiqi and R. Kishek, IEEE Trans. Electron Devices **66**(10), 4403 (2019).
[16] R. A. Kishek, Phys. Rev. Lett. **108**(3), 035003 (2012).
[17] S. Lin, R. Wang, N. Xia, Y. D. Li, and C. L. Liu, Phys. Plasmas **25**(1), 013536 (2018).
[18] H. Yang, W. Huang, B. Zeng, and H. Wen, IEEE Trans. Electron Devices **68**, 1918 (2021).
[19] L. Silvestre, Z. C. Shaw, T. Sugai, J. Stephens, J. J. Mankowski, J. Dickens, A. A. Neuber, and R. P. Joshi, J. Phys. D: Appl. Phys. **55**(4), 045202 (2022).
[20] J. Rasch and J. F. Johansson, Phys. Plasmas **19**(12), 123505 (2012).
[21] N. K. Vdovicheva, A. G. Sazontov, and V. E. Semenov, Radiophys. Quantum Electron. **47**(8), 580 (2004).
[22] S. Anza, C. Vicente, J. Gil, V. E. Boria, B. Gimeno, and D. Raboso, Phys. Plasmas **17**(6), 062110 (2010).
[23] S. Anza, M. Mattes, C. Vicente, J. Gil, D. Raboso, V. E. Boria, and B. Gimeno, Phys. Plasmas **18**(3), 032105 (2011).
[24] F. Shen, X. Wang, W. Cui, and L. Ran, IEEE Trans. Plasma Sci. **48**, 433 (2020).
[25] A. G. Sazontov and N. K. Vdovicheva, Appl. Phys. Lett **101**(11), 113506 (2012).
[26] E. Sorolla, A. Sounas, and M. Mattes, Phys. Plasmas **22**(3), 033512 (2015).
[27] V. E. Semenov, N. Zharova, R. Udiljak, D. Anderson, M. Lisak, and J. Puech, Phys. Plasmas **14**(3), 033509 (2007).
[28] S. V. Langellotti, N. M. Jordan, Y. Y. Lau, and R. M. Gilgenbach, IEEE Trans. Plasma Sci. **48**(6), 1942–1949 (2020).

[29]R. Udiljak, D. Anderson, M. Lisak, V. E. Semenov, and J. Puech, Phys. Plasmas **14**(3), 033508 (2007).
[30]S. Lin, H. Wang, Y. Li, C. Liu, N. Zhang, W. Cui, and A. Neuber, Phys. Plasmas **22**(8), 082114 (2015).
[31]S. Lin, P. Sun, Y. Li, H. Wang, and C. Liu, Phys. Plasmas **27**(2), 022115 (2020).
[32]V. D. Shemelin and S. A. Belomestnykh, *Multipactor in Accelerating Cavities* (Springer International Publishing, 2020).
[33]M. Furman and M. Pivi, Phys. Rev. Spec. Top. Accel. Beams **5**(12), 124404 (2002).
[34]C. Chang, J. Verboncoeur, S. Tantawi, and C. G. Jing, J. Appl. Phys. **110**(6), 063304 (2011).
[35]A. G. Sazontov, V. A. Sazontov, and N. K. Vdovicheva, Contrib. Plasma Phys. **48**(4), 331 (2008).
[36]ECSS Secretariat, Technical Report No. ECSS-E-20-01A Rev. 1, ESA-ESTEC Requirements and Standards Division, ESA-ESTEC, Noordwijk, The Netherlands, 2013.
[37]A. Woode and J. Petit, ESTEC Working Paper No. 1556, 1989.
[38]A. V. Gaponov and M. A. Miller, Sov. Phys. JETP **7**(3), 515 (1958).